ORIGINAL ARTICLE

Excavation-induced damage zoning of the underground powerhouse with high geostress based on multiple monitoring methods

Nuwen Xu[1] · Peiwei Xiao[1] · Biao Li[1] · Peng Li[1] · Yonghong Li[1] · Tieshuan Zhao[1] · Linlu Dong[1]

Abstract

The primary factor restricting the construction of deeply buried underground projects is the imprecise identification of the surrounding rock damage zone. This study examines the Shuangjiangkou underground powerhouse to investigate damage zoning in the surrounding rock mass. The temporal and spatial characteristics of deep rock mass deformation evolution are studied by multipoint extensometers, microseismic (MS) monitoring, acoustic wave testing and borehole TV. Subsequently, a quantitative analysis delineating damage zones is executed by evaluating alterations in displacement, wave velocity volatility, and the distribution of MS events within the surrounding rock mass. The excavation zone of the surrounding rock mass is segmented into distinct sectors: highly damaged zones (HDZs), excavation-damaged zones (EDZs) and excavation-disturbed zones (EdZs). Additionally, the energy ratio of S-waves to P-waves (E_s/E_p) and the moment tensor inversion (MTI) are introduced to reveal the failure mechanism of the surrounding rock mass in each damage zone. The results show that the rock mass fracture around the Shuangjiangkou underground powerhouse presents remarkable zonation characteristics. The spatial depth ranges for the HDZs, EDZs, and EdZs, determined quantitatively based on multivariate monitoring data, are 0–5 m, 5–10 m, and 10–20 m, respectively. The failure mechanisms of surrounding rock mass differ across various damage zones: the HDZ primarily exhibits tensile failure, while the EDZ is mainly characterized by shear failure. The research provides a valuable reference for evaluating the stability of surrounding rock during the excavation of underground caverns of Shuangjiangkou hydropower station.

Keywords Underground powerhouse · Multivariate monitoring · Deformation characteristics · Damage zoning · Failure mechanism

Introduction

China is actively developing hydropower stations in the southwest (Liang et al. 2020; Li et al. 2019). Arranging ground powerhouses is challenging due to geological constraints and construction requirements. Consequently, most large-scale hydropower projects are designed as underground installations (Xiao et al. 2022). Underground powerhouses are usually deeply buried and have high ground stress (Li et al. 2023). Extensive excavations commonly induce stress redistribution in the surrounding rock mass, resulting in rock loosening, cracking, and potential rock bursts, causing damage of varying extents (Li et al. 2020a).

For example, multiple collapses occurred while excavating the underground powerhouse at Baihetan hydropower station, significantly impacting the support system and posing substantial safety risks to construction workers (Xiao et al. 2016). Similar challenges were encountered at the Dagangshan (Shen et al. 2017), Wudongde (Li et al. 2018), Houziyan (Xiao et al. 2018) and Jinping II (Feng et al. 2015) hydropower stations. An imprecise comprehension of the extent of damage to the surrounding rock will elevate the engineering risk. Therefore, it is essential to categorize damage zones within high-stress underground caverns based on the extent of deterioration in the surrounding rock.

Numerous researchers employ field monitoring to analyse surrounding rock stability. Multipoint extensometers, digital measurement technology, 3D laser scanning, optical fibre monitoring, and MS monitoring find extensive applications in underground engineering construction. Feng et al. (2018) traced the deformation process of the rock mass using

✉ Nuwen Xu
 xunuwen@scu.edu.cn

[1] Sichuan University, Chengdu, China

multipoint extensometer testing, acoustic wave testing, and digital borehole photography. The deformation features of the tunnel were summarized by combining the monitoring data with theoretical analysis. Sato et al. (2000) compared the differences in damage to rock mass caused by mechanical excavation and blasting excavation with chromatographic measurements. The conclusion was that the extent of excavation damage was influenced by the method of excavation. Hata et al. (2023) designed enduring monitoring equipment to assess the safety of excavation damage zones (EDZs), offering a theoretical foundation for the secure geological disposal of radioactive waste. Liu et al. (2017) employed MS monitoring to observe and track the process of fault activation during excavation. The effectiveness of MS monitoring technology in risk identification of underground cavern excavation was proved.

Based on the differences in damage to the surrounding rock, zoning is conducive to reducing construction risk. Yan et al. (2015) categorized the excavation-induced damage zone of the Jinping II hydropower station into an internal damage zone and an external damage zone. The fracture pattern of the damaged zone was elucidated through a combination of field tests and numerical simulations. Cheng et al. (2017) utilized MS monitoring to investigate the distribution characteristics of vertical and horizontal damage in coal mine roofs and performed damage zoning. Xu et al. (2017) analysed the failure characteristics of underground cavern rock mass using multivariate monitoring methods and delineated potential risk areas. Mountaka et al. (2018) studied the formulation of the nonlinear constitutive model of rock mass and applied it to predict the expansion of the EDZs around the entrance. Verma et al. (2018) established the empirical correlation for the assessment of tunnel rock damage by field investigation data, and demonstrated the applicability of the empirical correlation through ultrasonic testing. Shi et al. (2022) analysed the influence of vehicle speed vibration on tunnel stability through numerical simulation. The risk zones of the tunnel were classified according to the damage to the surrounding rock.

It is of great significance to clarify the damage mechanism of rock mass to ensure the construction safety. In seismology, it is widely recognized that Es/Ep and MTI reveal the failure mechanism of earthquake sources. Cai et al. (1998, 2001, 2005) analysed 804 MS events in an underground engineering laboratory in Canada. The rock mass failure pattern revealed by E_s/E_p is basically consistent with the in-situ failure phenomenon. Xu et al. (2014)analysed the E_s/E_p characteristics of MS events on the left bank slope of the Jinping I hydropower station and combined them with numerical simulation to reveal the rupture pattern of the rock mass. Baker et al. (1997) delved into the failure mechanisms of individual seismic sources, revealing that tension-shear and contraction-shear dynamics play a role in initiating

source activity. Grosse et al. (2006) conducted indoor acoustic emission experiments and used moment tensor inversion to reveal rock failure patterns. Liu et al. (2015) investigated the damage of coarse-grained granite subjected to uniaxial compression through moment tensor analysis, aiding in comprehending the surrounding rock fracture characteristics in underground caverns.

This study aims to quantify damage zoning in high ground stress underground caverns and further elucidate failure mechanisms in distinct damage zones. This paper takes Shuangjiangkou underground powerhouse as the engineering background. Deformation features of the underground powerhouse are analysed using multipoint extensometers. The MS monitoring method is employed to acquire the development process of microfractures in the surrounding rock. Building upon the information above, the integration of acoustic wave testing and borehole TV is employed to conduct damage zoning of the surrounding rock. Subsequently, the E_s/E_p is introduced to determine the failure mechanism of the HDZ and the EDZ. Rupture patterns of microfractures in rocks are disclosed by the moment tensor inversion method.

Engineering background of the underground powerhouse

Project overview

The Shuangjiangkou hydropower station is located northwest of Chengdu, about 382 kms from the city. It is a crucial power project in the upper reaches of the Dadu River, and its primary function is to generate electricity. The station consists of four core structures: an earth-stone construction dam, one of the tallest in the world at 314 m, and three major systems for water diversion and power generation, flood discharge and diversion. The power generation system mainly comprises the main powerhouse, transformer chamber, tailrace surge chamber, and other vital parts. The overall layout of the underground cavern group is shown in Fig. 1.

Geological conditions of the underground powerhouse

The horizontal depth of the underground powerhouse is 400–640 m, and the vertical depth is 320–500 m. Composed primarily of granite, the rock mass is fresh and compact, exhibiting a saturated compressive strength of 60 MPa. Acoustic wave tests have indicated an average wave speed of 4500–5000 m/s, with certain pockets surpassing the 5000 m/s. The overall structural soundness of the rock mass at a depth of the powerhouse is robust, with some localized secondary fractures and joint fissures (Table 1).

**Fig. 1** Layout of the underground cavern group of the Shuangjiangkou hydropower station (Dong et al. 2023)
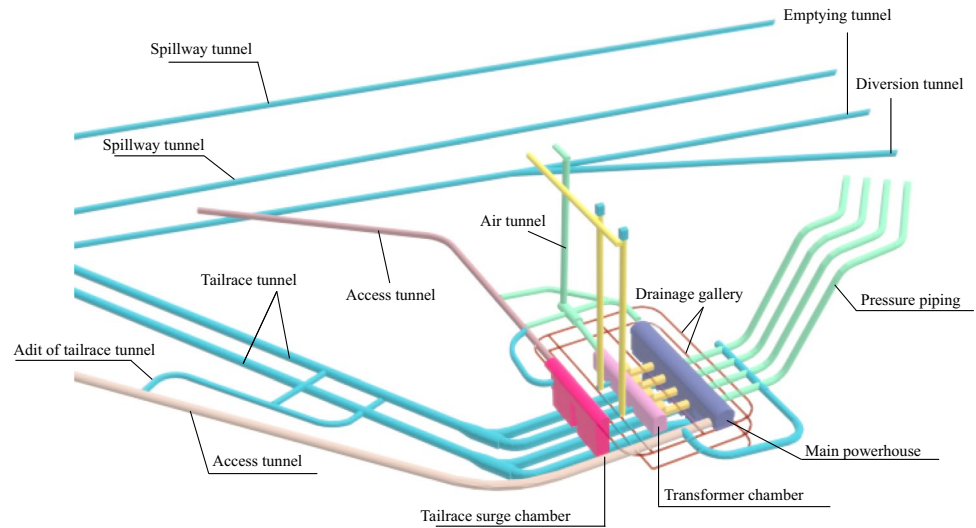
Table 1 Angle between the main fault fissures and joints and the longitudinal axis of the underground powerhouse (Dong et al. 2023)

Fault group no.	Strike	Dip direction	Dip angle	Crushing bandwidth (m)
SPD9-f1	N79°W	SW	∠48°	0.2–0.3
SPD9-f2	N33°W	NE	∠88°	0.5–0.6
Lamprophyre vein	N35°–50°W	SW	∠72°–75°	0.8–1.0
J1	N20°–50°E	SE	∠25°–42°	
J2	N5°–26°E	NW	∠10°–30°	
J3	N50°–75°W	SW	∠58°–75°	
J4	N60°–80°E	NW	∠5°–15°	
J5	N50°–60°E	SE	∠45°–65°	

Characteristics of geostress in the underground powerhouse

The valley at the dam site of the Shuangjiangkou hydropower station has an asymmetrical "*V*" shape. There is stress concentration at the bottom of the riverbed, and the maximum principal stress direction is close to the bank and parallel to the bank slope. There are 8 stress measurement points in the SPD9 adit of the underground powerhouse. The locations of the stress measurement points and the measurement results are detailed in Fig. 2 and Table 2. Based on analogous analyses with other hydropower underground stations, it is determined that Shuangjiangkou underground powerhouse has the highest ground stress level (Table 3). According to the evaluation of ground stress and the study of geological data, the ground stress distribution pattern of the Shuangjiangkou underground powerhouse shows apparent characteristics:
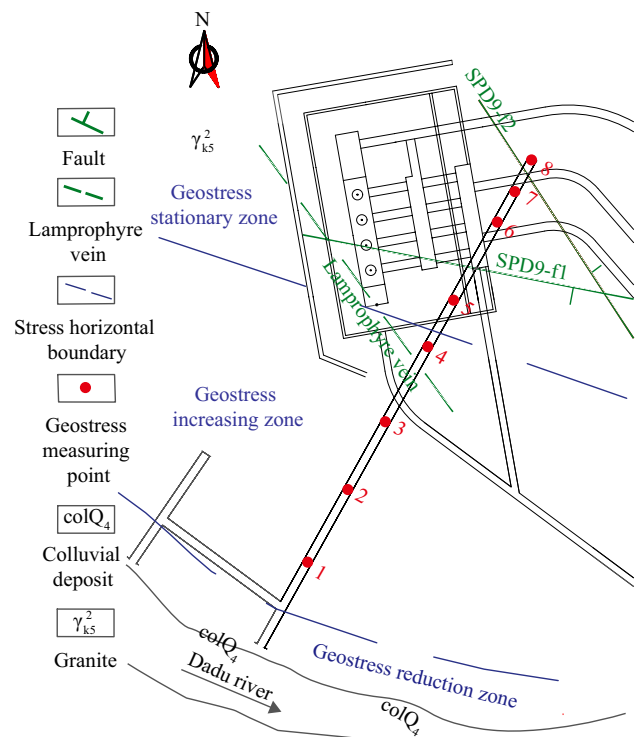
Fig. 2 Location of the rock mass geostress measuring points of the underground powerhouse (Elevation: 2264m) (Huang et al. 2022)

1. The orientation of the maximum principal stress is slightly disordered, with its dip angle close to horizontal.
2. The stress field within the underground powerhouse, influenced by plate tectonics, is primarily characterized by tectonic stress, complemented by gravity stress. The range of the maximum principal stress varies between 15.98 and 37.82 MPa, whereas the range of the minimum principal stress extends from 3.14 to 10.88 MPa.

Table 2 Geostress measurement results of the underground powerhouse zone (Huang et al. 2023)

Measuring point	Horizontal depth (m)	Vertical depth (m)	σ_1			σ_2			σ_3		
			Value (MPa)	α (°)	β (°)	Value (MPa)	α (°)	β (°)	Value (MPa)	α (°)	β (°)
1	115	107	15.98	325.6	30.1	8.53	81.8	37.3	3.14	208.5	38.1
2	205	173	22.11	332.0	30.1	11.63	84.0	32.9	5.86	210.1	42.3
3	301	238	19.21	323.0	-23.5	13.61	49.2	8.6	5.57	300.4	64.8
4	400	308	37.82	331.6	46.8	16.05	54.1	− 7.0	8.21	137.7	42.3
5	470	357	27.29	310.4	-3.5	18.27	36.8	45.6	8.49	223.8	44.2
6	540	431	16.91	357.0	19.0	10.32	92	14	8.01	216	66.0
7	570	470	28.96	325.0	27.2	18.83	72.5	30.3	10.88	201.4	47.0
8	640	549	24.56	349.0	18.0	20.37	92.0	35.0	10.52	237	49.0

Table 3 Representative underground powerhouses of large hydropower projects (Li et al. 2023)

Underground powerhouse	Excavation dimension (length × width × height) (m)	Vertical depth (m)	Maximum principal stress (MPa)	Lithology
Shuangjiangkou	219 × 28.3 × 68.3	320–500	15.98–37.82	Granite
Jinping I	277 × 29.2 × 68.7	180–420	20–35.7	Marble
Jinping II	352.4 × 28.3 × 72.2	300–470	10.1–22.9	Marble
Lianghekou	275.9 × 28.4 × 66.8	410–560	21.8–30.4	Metasandstone
Jinchuan	226.8 × 28.8 × 68.5	166–250	6–8	Metasandstone
Houziyan	219.5 × 29.2 × 68.7	400–660	21.6–36.4	Limestone
Changheba	147 × 30.8 × 73.4	285–480	16–32	Granite
Dagangshan	226.6 × 30.8 × 74.3	390–520	11.4–19.3	Granite

3. The ground stress exhibits a zoning phenomenon. Stress is released in a stress reduction zone at 0–45 m horizontal depth. In the 45–400 m, the maximum principal stress increases with depth, called the stress increasing zone. The peak stress value is 37.82 MPa at the horizontal depth of 400 m. Beyond the horizontal depth of 400 m, the maximum principal stress is 20–30 MPa, called the stress stationary zone.

Phenomenon of surrounding rock damage in the underground powerhouse

The side wall damage occurs frequently during the construction of the Shuangjiangkou underground powerhouse. Strong blasting disturbance lead to wedge failure and severe collapse near the lamprophyre dike upstream of the underground powerhouse, resulting in excavation stagnation for more than two months (see Fig. 3). The site investigation revealed that the damaged surface was relatively smooth and had longitudinal cracks. The collapse was mainly due to the intersection of structural surfaces. Figure 4 illustrates the damage to the remainder of underground chambers. There is variability in the damage pattern of the surrounding rock in different regions, such as cracking, rock spalling and wedge failure. The external surrounding rock failure is directly observable, while the deep rock mass state requires borehole TV detection. Figure 5 illustrates the progressive deterioration of the deep rock mass in borehole ZXCX4-1 upstream of the underground powerhouse over time.

Methodology

### Multiple monitoring methods

Multipoint extensometers

The surrounding rock deformation is a common issue during the construction of underground powerhouses. Multipoint extensometers monitoring was carried out to effectively monitor the deformation of the underground powerhouse. The specific monitoring arrangement is shown in Fig. 6. Figure 6a indicates a total of 6 monitoring sections in the underground powerhouse, and the stake number of section 6-6 is 0 + 135. This study mainly analyzes the stability of surrounding rock mass near the section 6-6. Figure 6b shows the layout of specific monitoring points in section 6-6 of the underground powerhouse.

Fig. 3 Collapse near section 6-6 at the upstream of the underground powerhouse
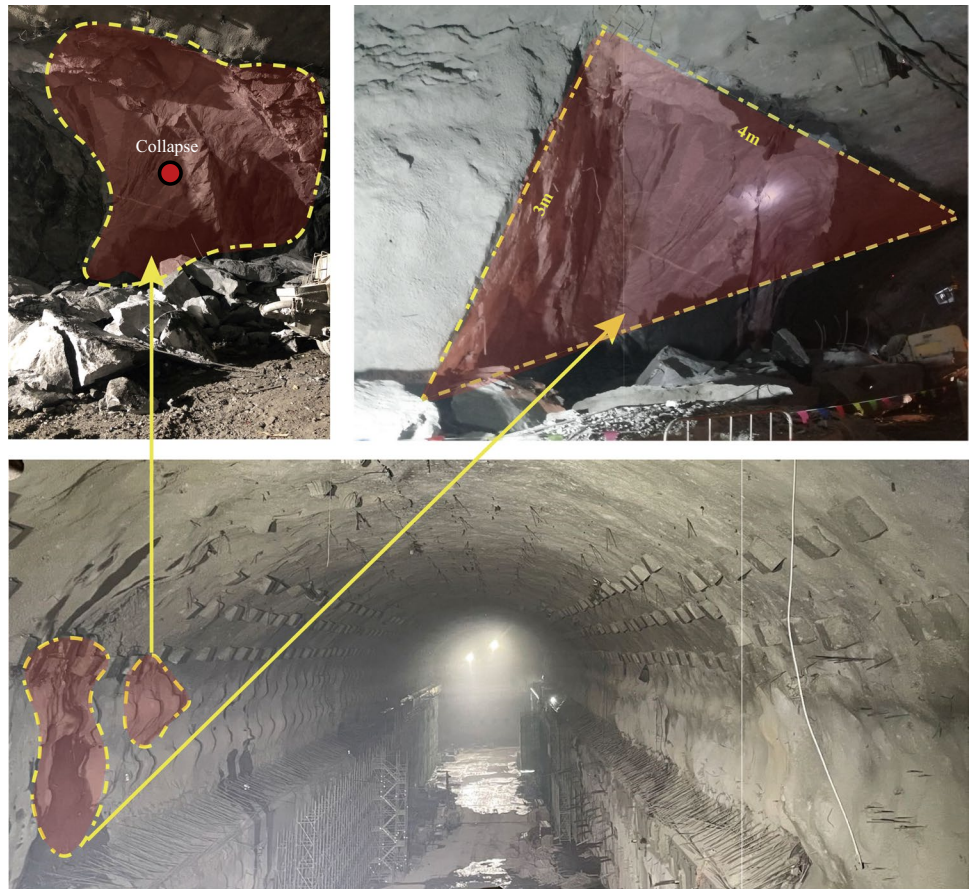
Fig. 4 Typical damage photos of the underground powerhouse area (Liang et al. 2020)
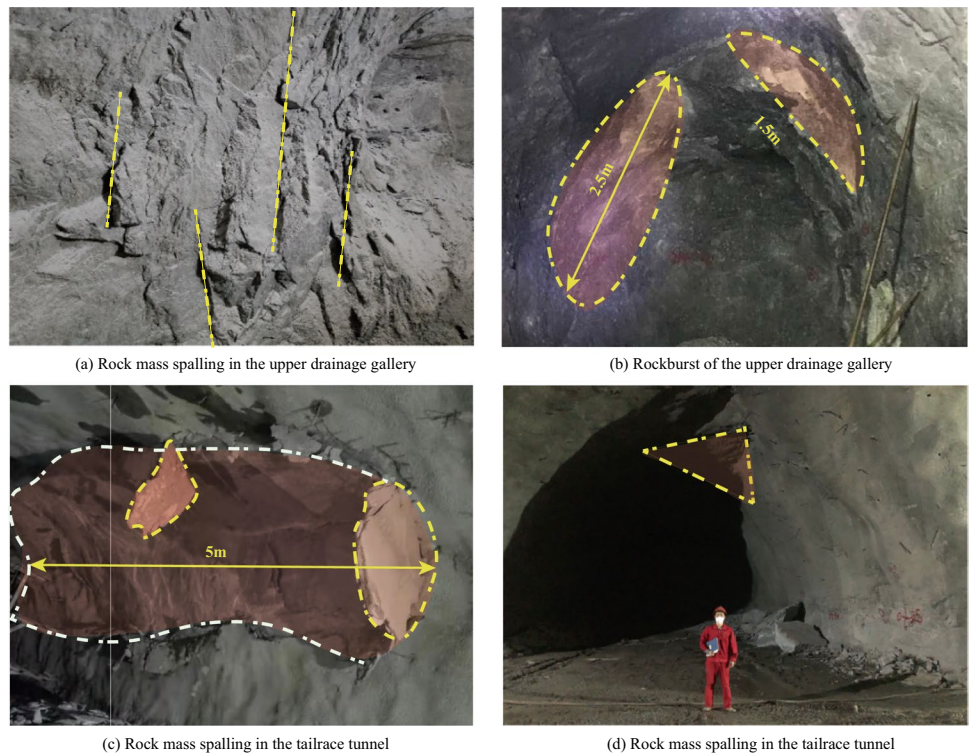
(a) Rock mass spalling in the upper drainage gallery

(b) Rockburst of the upper drainage gallery

(c) Rock mass spalling in the tailrace tunnel

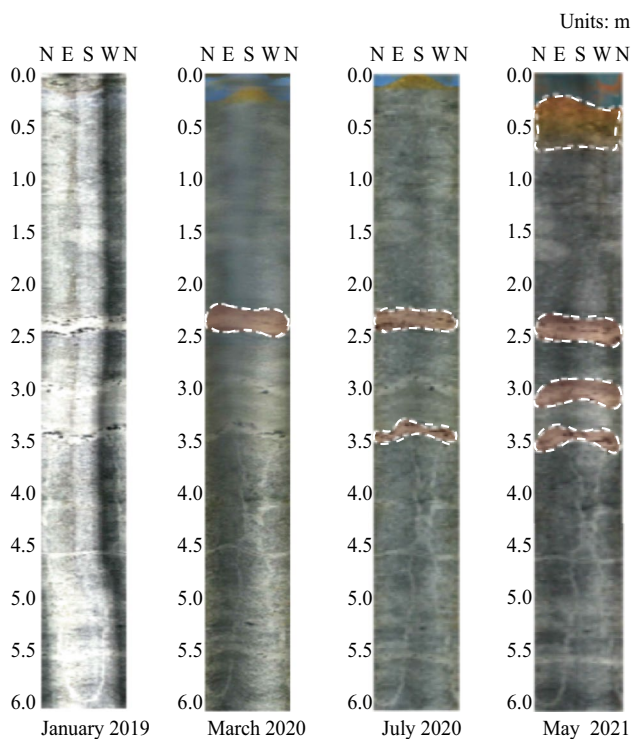(d) Rock mass spalling in the tailrace tunnel

Fig. 5 The ZXCX4-1 borehole TV image

MS monitoring

External disruptions alter the stress equilibrium within the rock mass, resulting in stress accumulation in specific zones. This causes microfractures within the rock mass and is accompanied by the emission of elastic waves. This type of elastic waves is geologically referred to as microseism (Zhang et al. 2021). MS monitoring has outstanding advantages and has been widely used in open-pit slopes (Xu et al. 2012; Dai et al. 2017), deep mines (Cao et al. 2016; Zhang et al. 2016; Li et al. 2021), hydropower stations (Huang et al. 2022; Li et al. 2022; Vikalp et al. 2019; Ma et al. 2022; Zhao et al. 2022), tunnels (Liu et al. 2020a; Xin et al. 2021; Chen et al. 2022) and other projects. This study discusses implementing MS monitoring techniques during the excavation stages of the underground powerhouse. The analysis of MS activity rate and energy release unveils the damage characteristics of the surrounding rock mass, offering a practical evaluation of its stability. Figure 7 illustrates the spatial arrangement of the sensors within the MS monitoring system used in the underground powerhouse. The detailed system establishment can be found in a previous study (Li et al. 2020b).
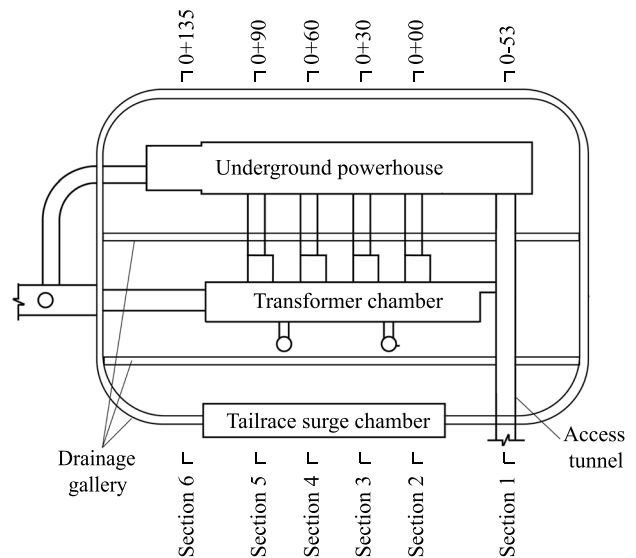
(a) Layout of monitoring sections
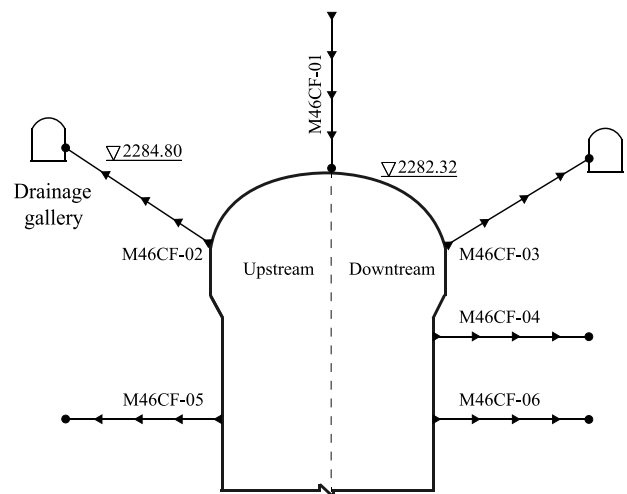
(b) Layout of monitoring points in section 6

Fig. 6 The monitoring layout

Acoustic wave testing and borehole TV

Acoustic wave testing uses acoustic velocity propagation in the medium to detect the internal defects of materials. The application of acoustic wave testing in underground engineering shows that wave velocity is positively correlated with the density of rock mass but negatively correlated with the degree of fracture development. Zones of high wave velocity indicate good rock mass integrity, while zones of low wave velocity indicate poor rock mass integrity. The results of acoustic wave testing serve as a criterion for categorizing the quality levels
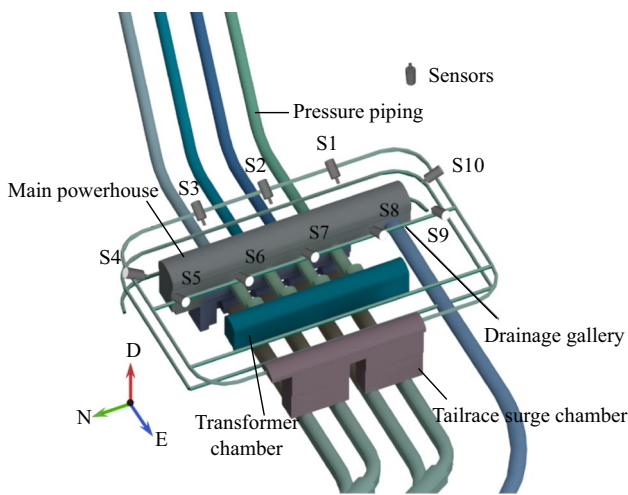
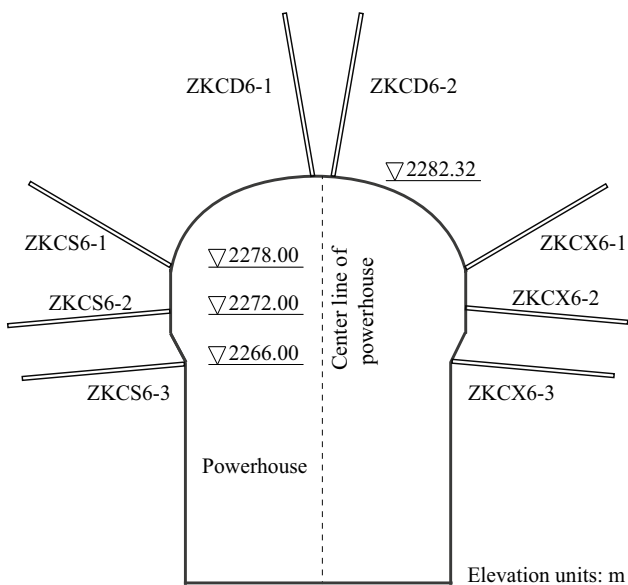**Fig. 7** Sensor layout of underground powerhouse (Li et al. 2020b)

Fig. 8 The layout of acoustic wave testing and borehole television detection for section 6-6

of rock mass. Borehole TV, a geophysical method, provides intuitive images of drill holes. It employs acoustic focusing and digital processing technologies to conduct in situ tests on advanced geological boreholes. This helps in identifying weak structural planes, such as joints and fissures. Borehole TV technology has wide applications in geological exploration and engineering geological detection (Li et al. 2011; Ma et al. 2020). Figure 8 illustrates the layout of acoustic wave testing and borehole television detection for section 6-6.

Failure mechanism analysis approach of surrounding rock mass

The value of ES/EP

The energy ratio of S waves to P waves (E_S/E_P) in seismology is a crucial indicator for revealing the failure mechanism of the surrounding rock mass (Liu et al. 2020b). The criteria for determining focal rupture mechanism based on E_S/E_P is described in Eq. (1). There is variability in the failure mechanisms of the surrounding rock in different zones. Therefore, independent analyses are carried out for the fracture patterns of the rock mass classified as HDZ and EDZ. When the E_S/E_P ratio is below 3, the rock failure is characterized by a predominance of tensile failure; when the E_S/E_P ratio is greater than 10, it exhibits predominantly shear failure; However, when the E_S/E_P ratio is between 3 and 10, the rock damage shows both tensile and shear failure modes, indicating the existence of mixed failure modes (Dai et al. 2016):

$$\begin{cases} ES/EP < 3, \text{ tensile failure} \\ 3 \leq ES/EP \leq 10, \text{ mixed failure} \\ ES/EP > 10, \text{ shear failure} \end{cases} \tag{1}$$

Moment tensor inversion

Seismic source mechanism analysis of engineering rock masses forms the foundation for monitoring and early warning systems in surrounding rock masses (Xu et al. 2021). Currently, research is actively focused on unveiling the seismic source mechanism using moment tensor theory. This involves decomposing the physical model with the moment tensor to create components, each bearing distinct mechanical properties. As Ohtsu (1995) elucidated, the mechanical characteristics of seismic sources are revealed by analysing the role of each component in the failure of rock masses.

Knopoff and Randall (1970) contributed significantly to this field by decomposing the moment tensor into three parts: an isotropic part (M^{ISO}), a compensating linear vector dipole (M^{CLVD}), and a double force couple (M^{DC}). These components correspond to expansion, tensile fracture, and shear dislocations, respectively. Building on this foundation, Ohtsu (1995) proposed a method to determine the mode of rock failure based on the proportion of M^{DC} relative to the three components, a method that has gained widespread recognition.

This paper incorporates the Ohstu's criterion to elucidate the source mechanism in rock masses. In the Cartesian coordinate system, the moment tensor (M) is represented by Eq. (2):

$$M = \begin{bmatrix} M_{11} & M_{12} & M_{13} \\ M_{21} & M_{22} & M_{23} \\ M_{31} & M_{32} & M_{33} \end{bmatrix}, \tag{2}$$

where M_{ij} represent the coupled forces acting in the opposite directions along the i and j axes. M must adhere to the principles of momentum conservation, thereby necessitating that M is a real symmetric matrix. In accordance with relevant elasticity theories, M must possess a principal stress direction, as expressed in Eq. (3):

$$M = \begin{bmatrix} M_1 & 0 & 0 \\ 0 & M_2 & 0 \\ 0 & 0 & M_3 \end{bmatrix}, \tag{3}$$

where M_1, M_2 and M_3 represent the principal stress tensors in three respective directions, obtainable by solving the eigenvalues of the moment tensor. Ohtsu (1995) interpreted the Acoustic Emission (AE) moment tensor from hydraulic fracturing tests as resulting from the interaction of M^{ISO}, M^{CLVD}, and M^{DC} components. The anisotropic principal stress is determined as the algebraic sum of these three components in their corresponding directions. Ohtsu decomposed the AE moment tensor, and the components of the three principal stresses are detailed in Eq. (4):

$$\begin{cases} M^{ISO} + M^{CLVD} + M^{DC} = M_1 \\ M^{ISO} - 0.5M^{CLVD} = M_2 \\ M^{ISO} - 0.5M^{CLVD} - M^{DC} = M_3 \end{cases}. \tag{4}$$

Ohtsu (1995) believes that $M^{ISO} \geq 0$, $M^{CLVD} \geq 0$, and $M^{DC} \geq 0$. Therefore, $M_1 \geq M_2 \geq M_3$. The eigenvalue of the AE moment tensor is calculated. M^{ISO}, M^{CLVD} and M^{DC} components can be obtained by substituting M_1, M_2 and M_3, respectively, according to the eigenvalues. Ohtsu used the dominance discrimination method to determine the type of failure based on the decomposition results (Eq. (5)):

$$P_{DC} = M^{DC}/(M^{ISO} + M^{CLVD} + M^{DC}). \tag{5}$$

Equation (5) demonstrates that the P_{DC} is constrained within the interval of 0 to 1. To precisely determine the failure mechanism of the surrounding rock mass, refer to Eq. (6):

$$\begin{cases} P_{DC} > 60\%, & \text{shear failure} \\ P_{ISO} < 40\%, & \text{tensile failure} \\ 40\% < P_{ISO} < 60\%, & \text{mixed failure} \end{cases}. \tag{6}$$

Results

Surrounding rock mass deformation

Figure 9 delineates the displacement–time progression curves obtained from multipoint extensometers at strategic locations on the top arch, and the upstream and downstream sidewalls of the underground powerhouse in section 6-6. The installation time of multipoint extensometers instrument is different and the deformation of the surrounding rock mass exhibits regional disparities. Therefore, the boundaries and units of the vertical axis are represented differently in each graphic. However, deformation trends at all monitoring sites can be summarized. The deformation pattern of the top arch and both sidewalls exhibits similarities, gradually reduced from the outside to the inside. The most significant displacement is noted at the orifice, underscoring the spatial variability of deformation within the structure. Significantly, the principal phase of deformation at the top arch was observed from late December 2018 to early January 2019, and again in mid-May 2019 (Fig. 9a). The deformation of the top arch orifice amounted to 14.32 mm, mainly due to the activation of the lamprophyre veins triggered by the strong disturbance of the excavation. Figure 9b–f illustrates that blasting excavations at various elevations in section 6-6 triggered abrupt displacement shifts in the sidewalls. The excavation near section 6-6 affected the multipoint extensometer data at the corresponding location, but the changes were minimal. However, the surrounding rock exhibits a more pronounced deformation if the excavation location coincides with the lamprophyre vein.

Figure 10 illustrates the displacement–hole depth process curve derived from multipoint extensometers in section 6-6. The excavation activity dramatically impacts the rock mass in the inner area of 3 to 5 m from the free surface, and the degree of deformation to the rock in this area is much greater than that of the deep rock mass. The rock mass deformation within a range of 5–10 m shows a gradual trend, while deformation in the 10–20 m remains relatively minor. The HDZ, EDZ and EdZ are defined based on the deformation and change rate of surrounding rock. The multipoint extensometers installed along the top arch and the upstream and downstream sidewalls of the underground powerhouse display comparable deformation trends. The deformation of different deep rock mass has obvious zoning phenomenon. Spatial deformation-based quantitative zoning of the surrounding rock offers a crucial reference point for devising the support structure for the underground powerhouse.

Surrounding rock mass failure

Figure 11 gives an overview of the daily MS events frequency and the average energy release of individual MS
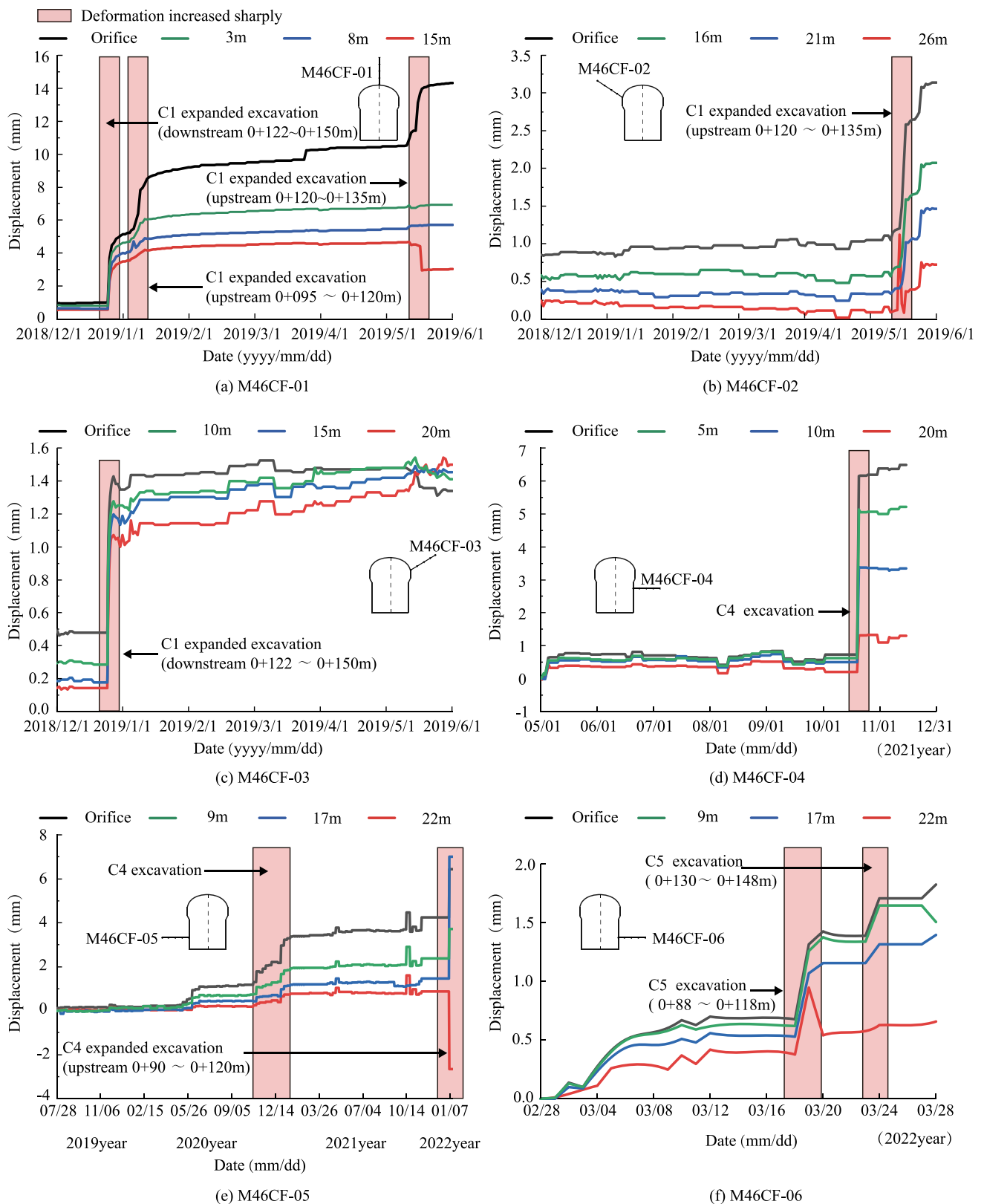
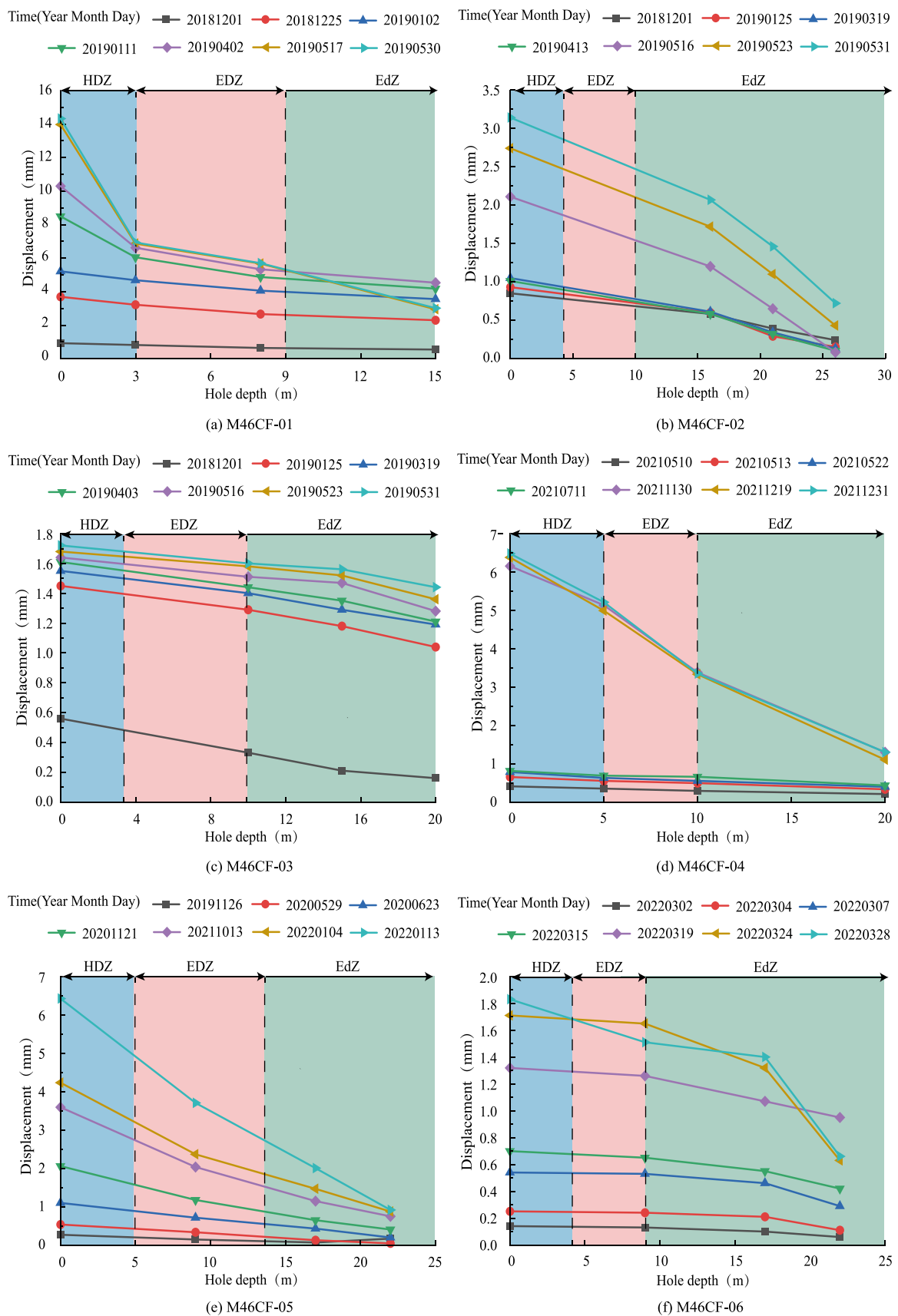**Fig. 9** The section 6-6 multipoint extensometers displacement–time process curve

Fig. 10 The section 6-6 multipoint extensometers displacement–hole depth process curve

events in May 2019. From the figure, it is evident that there were 98 MS events during this period, with an average of 3.2 events per day. There are two distinct phases based on the frequency of MS events. May 1–10 and May 20–31 were identified as the stage I. This phase featured a MS event frequency that was lower than average, predominantly attributed to shock wave impacts from blasting operations, which periodically altered stress within the surrounding rock formation. As a result, the average energy emitted by an individual MS event during this phase was comparatively low. May 11–19 were identified as the stage II, featured an average MS frequency of six, surpassing the overall average, and the average energy released per event was higher. In conjunction with the site study, it was found that a massive collapse occurred on May 17 at the lamprophyre vein upstream of the underground powerhouse. It is inferred that the increase in MS frequency is due to the sliding of the lamprophyre vein. This suggests that the increased MS frequency was due to the displacement of the brilliant porphyry vein. The disturbance to the unstable structural surface exacerbated the deterioration of the surrounding rock mass. Over time, this damage accumulated, culminating in a collapse that released a substantial amount of energy.

Figure 12 shows the spatial distribution and density cloud map of MS activity in the rock mass near section 6-6 of the powerhouse in May 2019. In this visualization, each sphere stands for a distinct microseismic event. The size of the sphere corresponds to the amount of energy radiated by the event: the larger the sphere, the more energy it represents. The color brightness of the sphere indicates the moment magnitude of the event, with brighter colors denoting higher magnitudes. Additionally, the presence of an energy density cloud acts as a visual representation of the density of the events, indicating how densely packed the energy is in a

given area. A significant concentration of MS activities was observed adjacent to section 6-6 along the upstream sidewall of the powerhouse. A total of 98 MS events were generated in May (Fig. 12d), including 25 MS events in the first week (Fig. 12a), 70 MS events in the first two weeks (Fig. 12b), and 87 MS events in the first three weeks (Fig. 12c). The MS frequency increases nonlinearly with time. Considering the moment magnitude and release energy of the MS events, it can be seen that large energy high magnitude events occur in the second week of May (Fig. 12b1). Field investigations indicated that the work programme for the second week of May was intensively worked in the vicinity of the Lamprophyre vein, which exacerbated the deterioration of the surrounding rock damage. The rock mass was subjected to a combination of cyclic excavation and poor structural surfaces that produced a large number of microfractures and strong manifestations of MS activity, which ultimately led to the collapse of the upper arch section. It is worth noting that the rock mass around the spandrel on the underground powerhouse collapsed on May 17, 2019. MS events continue to increase after the collapse, indicating that the stress adjustment damage of surrounding rock is still developing. As can be seen from Fig. 12d reveals that MS events are highly concentrated in the deep rock mass of the spandrel upstream of the underground powerhouse. Therefore, special attention should be paid to the surrounding rock state of the upstream spandrel.

Damage zoning of surrounding rock mass

Figure 13 presents the acoustic wave test results for section 6-6. Figure 13a and b depicts the acoustic test curves for the top arch at section 6-6. Within 3.0–4.0 m from the orifice, the rock mass exhibits a reduced wave speed, suggesting a comparatively unconsolidated structure, characteristic of a typical HDZ. This HDZ primarily results from the loosening of the lamprophyre vein due to excavation blasting vibrations. A comparison of Fig. 13a and b shows that ZKCD6-1, which is closer to the lamprophyre dyke, has a lower measured wave velocity than ZKCD6-2, indicating more extensive rock mass damage near the dyke. Figure 13c–e shows the acoustic testing curves in the upstream sidewall of section 6-6. The range from the orifice to 2.5–3.0 m is a low wave velocity zone of the rock mass. Severe unloading leads to significant damage to the surrounding rock. Thus, this zone is categorised as the HDZ. The wave velocity of the rock mass gradually increases within the range of 3.0–9.0 m. This indicates that the number of cracks in the surrounding rock is decreasing, defined as the EDZ. When the depth of the rock mass exceeds 9.0 m, the wave velocity is high and stable, reflecting a more structurally intact rock mass and can be classified as the EdZ.
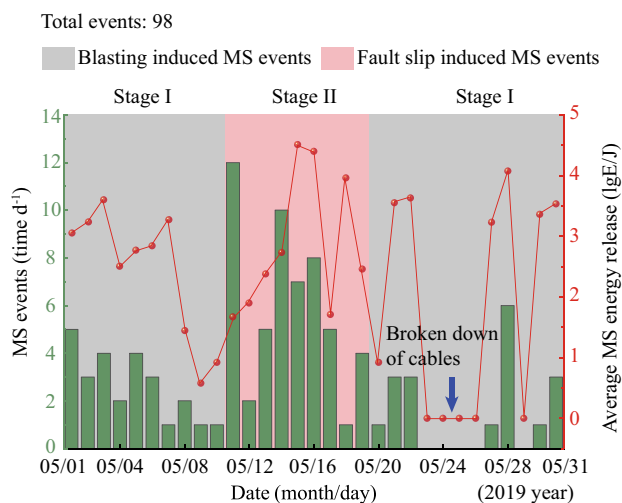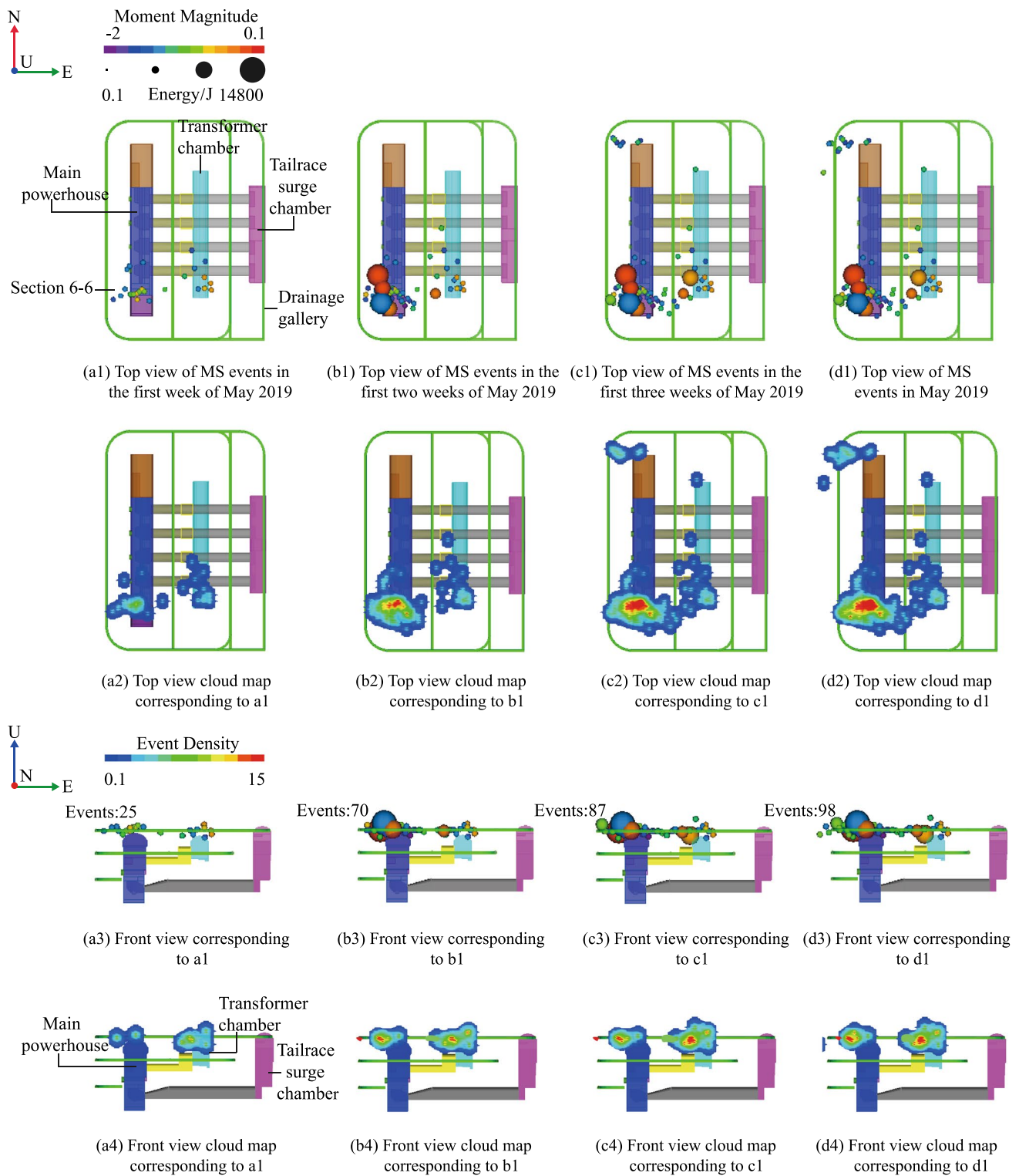

**Fig. 11** The change curve of MS activity rate and energy release

(a1) Top view of MS events in the first week of May 2019

(b1) Top view of MS events in the first two weeks of May 2019

(c1) Top view of MS events in the first three weeks of May 2019

(d1) Top view of MS events in May 2019

(a2) Top view cloud map corresponding to a1

(b2) Top view cloud map corresponding to b1

(c2) Top view cloud map corresponding to c1

(d2) Top view cloud map corresponding to d1

(a3) Front view corresponding to a1

(b3) Front view corresponding to b1

(c3) Front view corresponding to c1

(d3) Front view corresponding to d1

(a4) Front view cloud map corresponding to a1

(b4) Front view cloud map corresponding to b1

(c4) Front view cloud map corresponding to c1

(d4) Front view cloud map corresponding to d1

Fig. 12 Spatial distribution and density cloud map of MS events

Figure 14 shows the coordinated relationship of borehole TV image and multipoint extensometer in section 6-6. Figure 14a indicates that the hole depth of ZKCD6-1 is 20 m, in which the weak structural plane is in the range of 0.5 m, and the fault zone is in the range of 1.6 ~ 2.8 m. Joint fissures can be observed at 11.5 m, 12.2 m and 13.3 m. The rock mass in the rest of the hole is intact. Figure 14b shows the comparison between ZKCD6-1 borehole TV image and wave
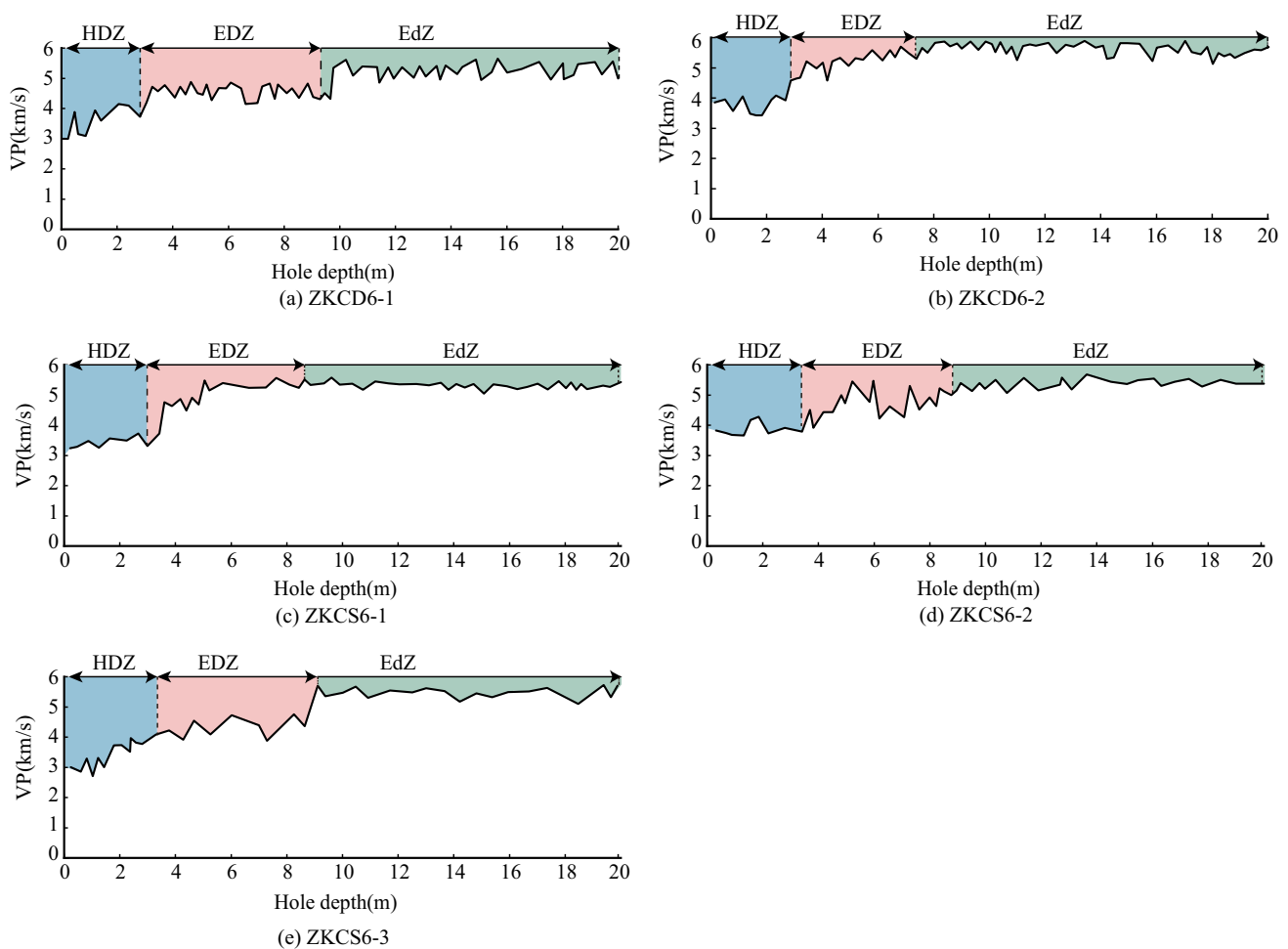
Fig. 13 Acoustic wave testing results at section 6-6

velocity. The borehole image shows that the fracture zone closely corresponds to the low-wave velocity zone of the surrounding rock in the range of 3 m. In the range of 16–20 m, the integrity of rock mass is better and the wave velocity of rock mass is higher. It can be seen that the borehole TV can directly display the occurrence state of rock mass structure and the high response of acoustic test results. Both of them provide an intuitive basis for the abnormal changes of physical parameters of rock mass.

Figure 15 shows a schematic diagram of the damaged zoning in section 6-6 of the underground powerhouse. It can be seen from the figure that in the MS gathering area, the surrounding rock deformation is large and the wave velocity of the rock mass is low, which jointly reveals the serious damage of the surrounding rock. Based on conventional and MS monitoring, the extent of damage to the underground powerhouse has been precisely defined. The HDZ mainly exists in the range of rock depth of 5 m, the EDZ is mainly distributed in the range of 5-10m, and the EdZ is mainly distributed in the range of 10-20m. The deep rock mass over

20 m is considered an undisturbed original rock. A comprehensive analysis of the wave velocity characteristics of the HDZ, EDZ and EdZ leads to the following conclusions. The velocity of acoustic waves through an undisturbed rock mass or EdZs ranges between 5100 and 5800 m/s. For the EDZ, this velocity typically lies between 4200 and 4800 m/s, with the attenuation rate of the velocity between 17 and 27%. In the HDZ, the acoustic wave velocity usually falls below 3800 m/s, and the attenuation rate lies between 25 and 34%. The combination of multiple monitoring methods supports delineating the damage zone of underground powerhouse excavations.

Surrounding rock mass failure patterns

Figure 16 displays the E_S/E_P values for the damaged zones of the surrounding rock mass. The colour of the sphere represents the failure pattern of the rock mass. The size of the sphere represents the logarithmic value of MS energy. As depicted in Fig. 16a, the HDZ in May 2019 primarily
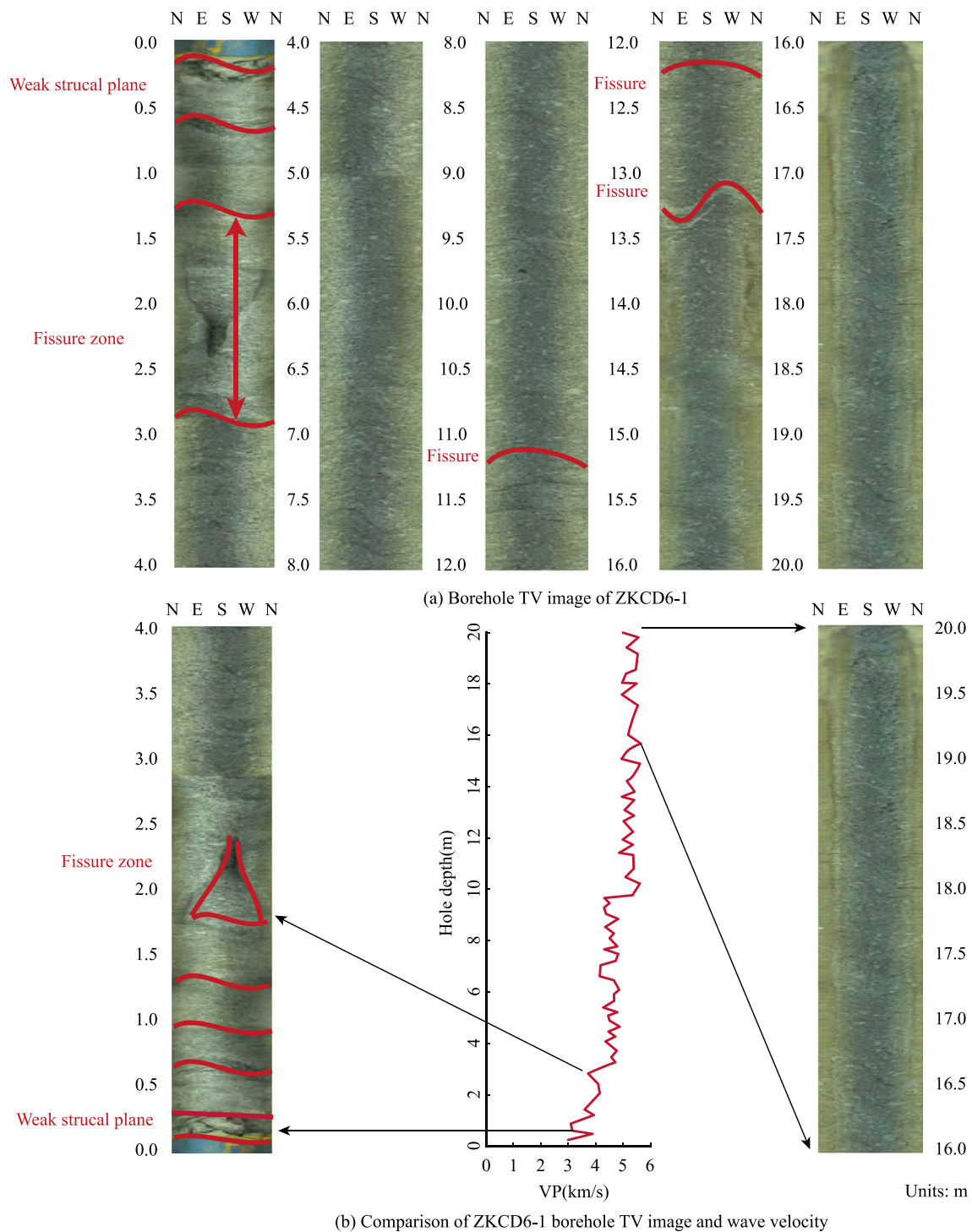
(a) Borehole TV image of ZKCD6-1

(b) Comparison of ZKCD6-1 borehole TV image and wave velocity

Fig. 14 The borehole TV images at section 6-6

exhibited tensile failures, with fewer shear failures. It was worth noting that the MS frequency near May 17 increased, and the MS energy release was significant. This coincides with the collapse of the powerhouse's upstream arch shoulder on May 17 (see Fig. 3). Preliminary analysis shows that the tensile failures in the HDZ are associated with tunnel

blasting. The blasting-generated shock waves significantly degrade the shallow surrounding rock mass. Repeated shock waves result in cyclic loading and unloading, leading to tensile failure in the rock mass. In contrast, Fig. 16b illustrates that in May 2019, the EDZ experienced predominantly shear and mixed failures, with a minor occurrence of
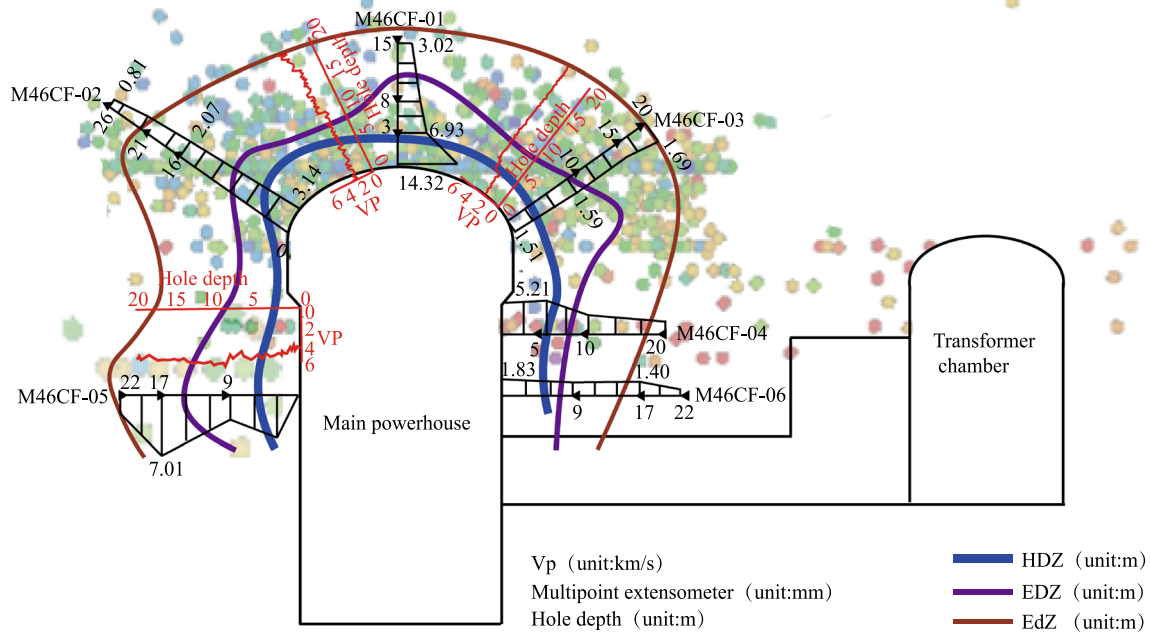
Fig. 15 Schematic diagram of the damaged zone at section 6-6 of the underground powerhouse (Reproduced from Xu et al. 2017)

tensile failures. Field investigation shows that the shear failure is related to the existence of lamprophyre dike, and the rock mass failure is caused by significant geological shear dislocation.

Figure 17 illustrates the failure mechanism of the MS events in May 2019. The failure mechanism of MS events exhibits obvious zoning characteristics. The zone near the powerhouse exhibits tensile failure. The side away from the powerhouse is characterized by shear failure. The transitional zone is characterized by mixed failure. It is further shown that the fracture patterns of the rock mass vary in different damage zones of the underground powerhouse. The source failure mechanism is highly similar to the results of E_S/E_P in determining the failure pattern of the HDZ and EDZ.

Discussion

The surrounding rock mass, characterized by its high stress, intense disturbance, and complex geological conditions, is prone to substantial deformation and failure. Numerous theoretical studies and engineering practices demonstrate that surrounding rock damage zone broadly categorized into three types: HDZ, EDZ, and EdZ (Xu et al. 2017). There may be different failure modes in different damage zones,

such as tensile failure, shear failure and mixed failure. The tectonic plane in rock mass is an important factor affecting the failure mode of rock mass.

The disturbance caused by excavation destroys the integrity of surrounding rock and causes its physical state to change. The damage zone is determined based on the state characteristics of surrounding rock. This study used multiple monitoring to find that the HDZ is primarily affected by blasting. The shock wave produced by blasting has obvious destructive effect on shallow buried surrounding rock. The disturbance causes the surrounding rock to break, and the damage gradually accumulates and causes large deformation. The EDZ is mainly affected by lamprophyre vein slip, which reduces the strength of rock mass.

The E_S/E_P is used to further determine the failure mode of rock mass. The repeated shock wave of blasting vibration leads to cyclic loading and unloading, resulting in tensile failure of shallow rock mass. The stress adjustment induced by external disturbance makes the deep lamprophyre vein slide to adapt to the environment. This failure mode is consistent with the E_S/E_P statistics and the result of moment tensor inversion. The results based on moment tensor inversion show that the shallow rock mass is mostly tensile damage, and the deep rock mass exhibits shear damage.

This study used a multidimensional monitoring method to delineate the surrounding rock damage zone. The HDZ
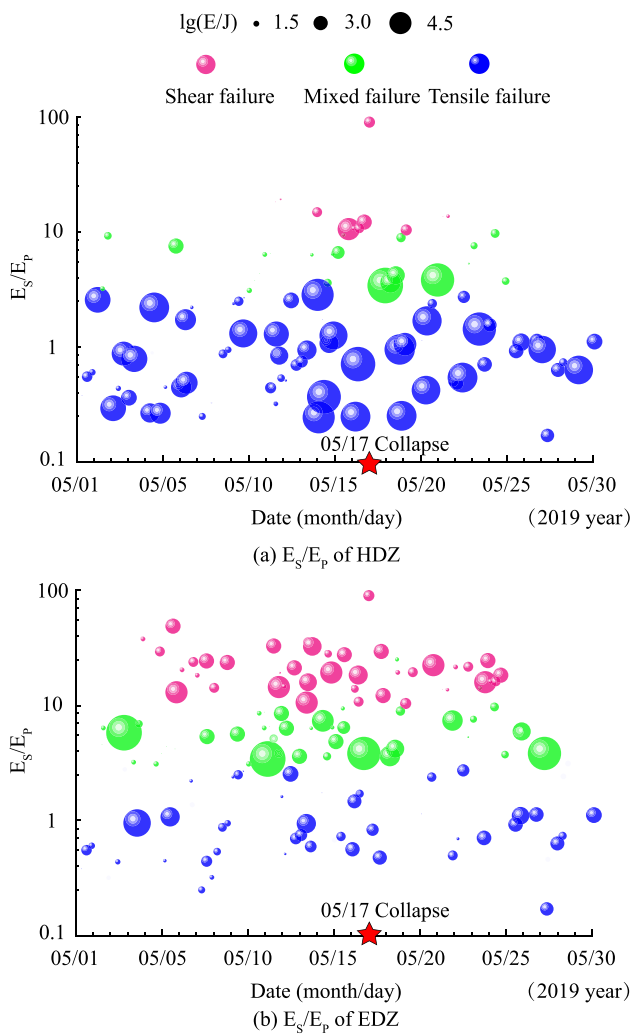
Fig. 16 The E_S/E_P of the surrounding rock mass damaged zone

Fig. 17 Seismic source failure mechanism in the main powerhouse

is a shallow rock mass with a depth of 5 m or less, which mainly exhibits tensile failure, and the EDZ is a rock mass with a depth of 5–10 m, which mainly exhibits shear failure. The obtained results provide certain reference for support and safety warning.

Conclusions

In the present study, multiple monitoring methods including multipoint extensometers, MS monitoring, acoustic wave testing, and borehole TV were employed to quantitatively identify the damage zoning of surrounding rock mass of the underground powerhouse in Shuangjiangkou hydropower station. The failure mechanism of surrounding rock mass in the different damage zones was revealed through the Es/Ep and MTI. The main conclusions can be drawn:

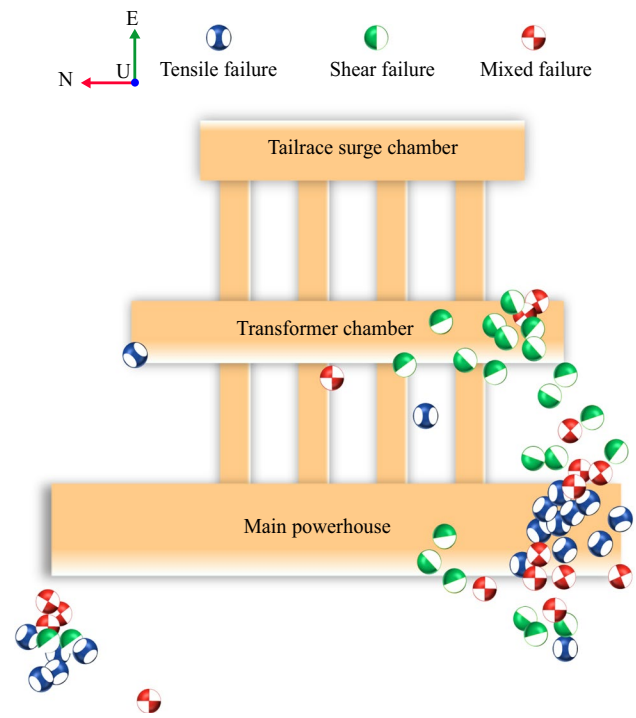1. This study found that the deformation of the surrounding rock of the underground powerhouse at the Shuangjiangkou hydropower station exhibits obvious zonal characteristics, as determined by a multiple monitoring method. The damage zone of surrounding rock is quantitatively divided by monitoring data. The HDZ depth is less than 5 m in shallow rock mass, the EDZ depth is 5–10 m, and the EdZ depth is 10–20 m.

2. There are discrepancies in wave velocity across different damage zones of the underground powerhouse at the Shuangjiangkou hydropower station. In the EdZ, wave velocities typically range between 5100 and 5800 m/s. For the EDZ, the wave velocities are generally between 4200 and 4800 m/s. In the HDZ, wave velocities usually fall below 3800 m/s.

3. The failure mechanisms of the surrounding rock mass vary among the different damage zones of the underground powerhouse of the Shuangjiangkou hydropower station. The surrounding rock of HDZ mainly exhibits tensile failure due to its Es/Ep value less than 3. However, the Es/Ep value of EDZ surrounding rock is greater than 3, which mainly shows shear failure.

4. The quantitative zoning of surrounding rock damage based on multiple monitoring methods can provide guidance for the support design of Shuangjiangkou underground powerhouse. The Es/Ep and moment tensor inversion methods reveal the failure mode of surround-

ing rock, which can provide reference for the safety warning of Shuangjiangkou underground caverns.

Data availability No datasets were generated or analysed during the current study.

Declarations

Conflict of interest The authors declare no competing interests.

References

C Baker RP Young 1997 Evidence for extensile crack initiation in point source time-dependent moment tensor solutions Bull Seismol Soc Am 87 6 1442 1453 https://doi.org/10.1785/BSSA0870061442

M Cai PK Kaiser 2005 Assessment of excavation damaged zone using a micromechanics model Tunn Undergr Space Technol 20 301 310 https://doi.org/10.1016/j.tust.2004.12.002

M Cai PK Kaiser CD Martin 1998 A tensile model for the interpretation of microseismic events near underground openings Pure Appl Geophys 153 1 67 92 https://doi.org/10.1007/978-3-0348-8804-2_5

M Cai PK Kaiser CD Martin 2001 Quantification of rock mass damage in underground excavations from microseismic event monitoring Int J Rock Mech Min Sci 38 8 1135 1145 https://doi.org/10.1016/S1365-1609(01)00068-5

AY Cao LM Dou CB Wang CB Wang XX Yao JY Dong Y Gu 2016 Microseismic precursory characteristics of rock burst hazard in mining areas near a large residual coal pillar: a case study from Xuzhuang coal mine, Xuzhou China Rock Mech Rock Eng 49 11 4407 4422 https://doi.org/10.1007/s00603-1037-7

YY Chen PW Xiao P Li X Zhou ZZ Liang NW Xu 2022 Formation mechanism of rockburst in deep tunnel adjacent to faults: implication from numerical simulation and microseismic monitoring J Central South Univ 29 12 4035 4050 https://doi.org/10.1007/s11771-022-5211-6

GW Cheng TH Ma CA Tang HY Liu SJ Wang 2017 A zoning model for coal mining—induced strata movement based on microseismic monitoring Int J Rock Mech Min Sci 94 123 138 https://doi.org/10.1016/j.ijrmms.2017.03.001

F Dai B Li NW Xu YL Fan CQ Zhang 2016 Deformation forecasting and stability analysis of large-scale underground powerhouse caverns from microseismic monitoring Int J Rock Mech Min Sci 86 269 281 https://doi.org/10.1016/j.ijrmms.2016.05.001

F Dai B Li NW Xu GT Meng JY Wu YL Fan 2017 Microseismic monitoring of the left bank slope at the Baihetan hydropower station China Rock Mech Rock Eng 50 1 225 232 https://doi.org/10.1007/s00603-016-1050-9

LL Dong P Li YH Li TS Zhao YP Sun PW Xiao XG Yang 2023 Mechanical response and stability analysis of surrounding rock mass during roof arch excavation of underground powerhouse under high in-situ stress Chin J Rock Mech Eng 42 5 1096 1109 https://doi.org/10.13722/j.cnki.jrme.2022.0925

GL Feng XT Feng BR Chen YX Xiao Y Yu 2015 A microseismic method for dynamic warning of rockburst development processes in tunnels Rock Mech Rock Eng 48 5 2061 2076 https://doi.org/10.1007/s00603-014-0689-3

XT Feng ZB Yao SJ Li SY Wu CX Yang HS Guo S Zhong 2018 In situ observation of hard surrounding rock displacement at 2400-m-deep tunnels Rock Mech Rock Eng 51 3 873 892 https://doi.org/10.1007/s00603-017-1371-3

CU Grosse F Finck 2006 Quantitative evaluation of fracture processes in concrete using signal-based acoustic emission techniques Cement Conc Compos 28 4 330 336 https://doi.org/10.1016/j.cemconcomp.2006.02.006

K Hata N Sumio A Kazuhei M Nobukatsu 2023 Evaluation of excavation damaged zones (EDZs) in Horonobe Underground Research Laboratory (URL) J Rock Mech Geotech Eng https://doi.org/10.1016/j.jrmge.2023.05.010

X Huang NW Xu W Wu PW Xiao LL Dong B Li 2022 Instability of an intersecting fault-dyke system during deep rock excavation Int J Rock Mech Min Sci 153 105087 https://doi.org/10.1016/j.ijrmms.2022.105087

L Knopoff MJ Randall 1970 The compensated linear-vector dipole: a possible mechanism for deep earthquakes J Geophys Res 75 26 4957 4963 https://doi.org/10.1029/JB075i026p04957

SJ Li XT Feng ZH Li BR Chen Q Jiang SY Wu B Hu JS Xu 2011 In situ experiments on width and evolution characteristics of excavation damaged zone in deeply buried tunnels Sci China Technol Sci 54 1 167 174 https://doi.org/10.1007/s11431-011-4637-0

A Li NW Xu F Dai GK Gu ZH Hu Y Liu 2018 Stability analysis and failure mechanism of the steeply inclined bedded rock masses surrounding a large underground opening Tunn Undergr Space Technol 77 45 58 https://doi.org/10.1016/j.tust.2018.03.023

B Li NW Xu F Dai GL Zhang PW Xiao 2019 Dynamic analysis of rock mass deformation in large underground caverns considering microseismic data Int J Rock Mech Min Sci 122 104078 https://doi.org/10.1016/j.ijrmms.2019.104078

B Li NW Xu F Dai GK Gu W Ke 2020a Microseismic monitoring and stability analysis for the large-scale underground caverns at the Wudongde hydropower station Bull Eng Geol Env 79 7 3559 3573 https://doi.org/10.1007/s10064-020-01777-z

B Li QF Ding NW Xu YF Lei Y Xu ZP Zhu JF Liu 2020b Mechanical response and stability analysis of rock mass in high geostress underground powerhouse caverns subjected to excavation J Central South Univ 27 10 2971 2984 https://doi.org/10.1007/s11771-020-4522-8

N Li LL Fang WC Sun X Zhang D Chen 2021 Evaluation of borehole hydraulic fracturing in coal seam using the microseismic monitoring method Rock Mech Rock Eng 54 2 607 625 https://doi.org/10.1007/s00603-020-02297-8

B Li QF Ding NW Xu F Dai Y Xu HL Qu 2022 Characteristics of microseismic b-value associated with rock mass large deformation in underground powerhouse caverns at different stress levels J Central South Univ 29 2 693 711 https://doi.org/10.1007/s11771-022-4946-4

B Li NW Xu PW Xiao Y Xia X Zhou GK Gu XG Yang 2023 Microseismic monitoring and forecasting for dynamic disasters in underground hydropower projects in southwest China: a review

J Rock Mech Geotech Eng 15 8 2158 2177 https://doi.org/10.1016/j.jrmge.2022.10.017

ZZ Liang RX Xue NW Xu LL Dong YH Zhang 2020 Analysis on microseismic characteristics and stability of the access tunnel in the main powerhouse, Shuangjiangkou hydropower station, under high in situ stress Bull Eng Geol Env 79 6 3231 3244 https://doi.org/10.1007/s10064-020-01738-6

JP Liu YH Li SD Xu S Xu CY Jin 2015 Cracking mechanisms in granite rocks subjected to uniaxial compression by moment tensor analysis of acoustic emission Theoret Appl Fract Mech 75 151 159 https://doi.org/10.1016/j.tafmec.2014.12.006

C Liu SG Li C Cheng JH Xue 2017 Activation characteristics analysis on concealed fault in the excavating coal roadway based on microseismic monitoring technique Int J Min Sci Technol 27 5 883 887 https://doi.org/10.1016/j.ijmst.2017.06.023

JP Liu YT Si CY Zhang R Wang 2020a Estimation of fracturing mechanisms by the ratio of radiated energy between S and P waves of microseismic events during mining in metal mines Appl Geophys 17 03 465 474 https://doi.org/10.1007/s11770-020-0856-0

QS Liu J Wu XP Zhang LX Tang C Bi WW Li JL Xu 2020b Microseismic monitoring to characterize structure-type rockbursts: a Case Study of a TBM-Excavated tunnel Rock Mech Rock Eng 53 7 2995 3013 https://doi.org/10.1007/s00603-020-02111-5

K Ma JH Zhang Z Zhou NW Xu 2020 Comprehensive analysis of the surrounding rock mass stability in the underground caverns of Jinping I hydropower station in Southwest China Tunn Undergr Space Technol 104 103525 https://doi.org/10.1016/j.tust.2020.103525

K Ma XY Sun ZH Zhang J Hu ZR Wang 2022 Intelligent Location of microseismic events based on a fully convolutional neural network (FCNN) Rock Mech Rock Eng 55 8 4801 4817 https://doi.org/10.1007/s00603-022-02911-x

S Mountaka R Vincent AH Marwan B Christian L Franz N Anders 2018 Numerical investigation of the development of the excavation damaged zone around a deep polymetallic ore mine Int J Rock Mech Min Sci 106 165 175 https://doi.org/10.1016/j.ijrmms.2018.04.028

M Ohtsu 1995 Acoustic emission theory for moment tensor analysis Res Nondestr Eval 6 3 169 184 https://doi.org/10.1007/BF01606380

T Sato T Kikuchi K Sugihara 2000 In-situ experiments on an excavation disturbed zone induced by mechanical excavation in Neogene sedimentary rock at Tono mine, central Japan Eng Geol 56 97 108 https://doi.org/10.1016/S0013-7952(99)00136-2

YJ Shen GL Xu JN Yi 2017 A systematic engineering geological evaluation of diabase dikes exposed at the underground caverns of Dagangshan hydropower station Southwest China Environ Earth Sci 76 481 https://doi.org/10.1007/s12665-017-6806-3

CH Shi SXH WangA WC Yang 2022 Research on the movement law and traffic safety zoning of spalled blocks in the linings of high-speed railway tunnels Tunn Undergr Space Technol 128 104614 https://doi.org/10.1016/j.tust.2022.104614

HK Verma NK Samadhiya M Singh RK Goel PK Singh 2018 Blast induced rock mass damage around tunnels Tunnel Undergr Space Technol 71 149 158 https://doi.org/10.1016/j.tust.2017.08.019

K Vikalp N Gopalakrishnan NP Singh C Sivakumar 2019 Microseismic monitoring application for primary stability evaluation of the powerhouse of the Tapovan Vishnugad Hydropower Project J Earth Syst Sci 128 6 169 https://doi.org/10.1007/s12040-019-1191-9

YX Xiao XT Feng GL Feng HJ Liu Q Jiang SL Qiu 2016 Mechanism of evolution of stress-structure controlled collapse of surrounding rock in caverns: a case study from the Baihetan hydropower station in China Tunn Undergr Space Technol 51 56 67 https://doi.org/10.1016/j.tust.2015.10.020

XH Xiao PW Xiao F Dai HB Li XB Zhang JW Zhou 2018 Large deformation characteristics and reinforcement measures for a rock pillar in the Houziyan underground powerhouse Rock Mech Rock Eng 51 2 561 578 https://doi.org/10.1007/s00603-017-1329-5

PW Xiao HY Mao B Qian B Li XG Yang NW Xu 2022 Stability analysis of surrounding rock mass in underground powerhouse considering damage effect of microfractures J Rock Mech Geotech Eng 14 4 1115 1130 https://doi.org/10.1016/j.jrmge.2022.01.007

Y Xin QS Liu YC Pan X Huang 2021 A novel tree-based algorithm for real-time prediction of rockburst risk using field microseismic monitoring Environ Earth Sci 80 16 504 https://doi.org/10.1007/s12665-021-09802-4

NW Xu CA Tang H Li F Dai K Ma JD Shao JC Wu 2012 Excavation-induced microseismicity: microseismic monitoring and numerical simulation J Zhejiang Univ Sci A 13 6 445 460 https://doi.org/10.1631/jzus.A1100131

NW Xu F Dai ZZ Liang Z Zhou C Sha CA Tang 2014 The dynamic evaluation of rock slope stability considering the effects of microseismic damage Rock Mech Rock Eng 47 2 621 642 https://doi.org/10.1007/s00603-013-0432-5

NW Xu F Dai B Li YG Zhu T Zhao DS Yang 2017 Comprehensive evaluation of excavation-damaged zones in the deep underground caverns of the Houziyan hydropower station, Southwest China Bull Eng Geol Env 76 1 275 293 https://doi.org/10.1007/s10064-016-0858-6

ZG Xu SS Liang N Mohd HW Li JY Shi 2021 Historical earthquakes, tsunamis and real-time earthquake monitoring for tsunami advisory in the South China Sea region Nat Hazards 107 1 771 793 https://doi.org/10.1007/s11069-021-04605-z

P Yan WB Lu M Chen YG Hu CB Zhou XX Wu 2015 Contributions of In-situ stress transient redistribution to blasting excavation damage zone of deep tunnels Rock Mech Rock Eng 48 2 715 726 https://doi.org/10.1007/s00603-014-0571-3

PH Zhang TH Yang QL Yu T Xu WH Shi SC Li 2016 Study of a seepage channel formation using the combination of microseismic monitoring technique and numerical method in Zhangmatun iron mine Rock Mech Rock Eng 49 9 3699 3708 https://doi.org/10.1007/s00603-016-1007-z

YB Zhang XL Yao P Liang KX Wang L Sun BZ Tian XX Liu SY Wang 2021 Fracture evolution and localization effect of damage in rock based on wave velocity imaging technology J Central South Univ 28 2752 2769 https://doi.org/10.1007/s11771-021-4806-7

JS Zhao BR Chen Q Jiang JF Lu XJ Hao SF Pei F Wang 2022 Microseismic monitoring of rock mass fracture response to blasting excavation of large underground caverns under high geostress Rock Mech Rock Eng 55 2 733 750 https://doi.org/10.1007/s00603-021-02709-3